Substrate temperature effects on laser crystallized NiTi thin films

A. J. Birnbaum,[1,a] Ui-Jin Chung,[2] X. Huang,[3] James S. Im,[2] A. G. Ramirez,[3] and Y. L. Yao[1]
[1]*Mechanical Engineering Department, Columbia University, New York, New York 10027, USA*
[2]*Department of Applied Physics and Applied Mathematics, Program in Materials Science, Columbia University, New York, New York 10027, USA*
[3]*Mechanical Engineering Department, Yale University, New Haven, Connecticut 06511, USA*

(Received 26 September 2008; accepted 28 January 2009; published online 1 April 2009)

Amorphous sputter-deposited NiTi thin films were subjected to pulsed, melt-mediated laser crystallization techniques to engineer their microstructure. The effects of laser processing of preheated films are examined. Laser processing of films at an elevated substrate temperature has a significant effect on the rate with which solidification occurs. It is observed that the preheating temperature at which processing is carried out has significant implications for the resulting phase and microstructure, and therefore mechanical properties. Furthermore, the microstructural effects of varying incident laser energy density are examined via atomic force microscopy, scanning electron microscopy, and x-ray diffraction, and mechanical/shape memory properties are characterized via nanoindentation. © *2009 American Institute of Physics*. [DOI: 10.1063/1.3093678]

I. INTRODUCTION

Pulsed, melt-mediated laser crystallization techniques have been studied extensively for a range of material classes including semiconductors, and elemental and alloyed metals.[1–3] The process provides a flexible means for spatial control over crystalline/amorphous regions as well as a high degree of control over the resulting microstructure itself. By controlling melting and solidification and patterned film (or beam) geometries, grain size and shape as well as texture may be specifically tailored toward a range of applications.[2,4] Silicon thin films have been processed in this manner for the production of thin film transistors for use in active matrix displays (e.g., Liquid Crystal Display (LCD) and Organic Light Emitting Diode (OLED)). These applications also rely on the ability of the process for controlling the density of microstructural defects (e.g., high-angle grain boundaries) which have significant effects on device performance.[4,5] Spaepen and co-workers[6–8] used the pulsed melt-mediated process to produce and study the behavior of thin film metallic glasses and thin film metallic alloys. This process is well suited toward this end owing to exceedingly high quench rates.[7] Interest in processing elemental metals has also increased as a means for producing and tailoring microstructures for interconnects in Integrated Circuits (IC) circuitry.[9]

Pulsed, melt-mediated laser crystallization techniques have yet to be utilized in processing thin film shape memory alloys (SMAs) but hold definite potential for control over the resulting structure. Although SMAs' nonconventional properties have been studied extensively over the last 4 decades, their actual implementation has been limited due to several complicating factors. A main impediment to application, particularly for thermally induced macroscale actuation applications, is poor dynamic response stemming from long heat dissipation times. Recently, thin film shape memory structures have received increasing attention for microscale actuation as they do not suffer from this limitation due to their exceedingly low thermal mass. In addition to the shape memory effect, significant attention has also been devoted to exploiting the superelastic effect. In particular, applications in improving the wear resistance of NiTi surfaces have received increasing amounts of interest.[10–12]

The majority of this work has examined thin films whose shape memory properties are homogeneous throughout the film. Ishida *et al.*[13–15] conducted a series of in depth investigations on the effects of furnace, solid-phase crystallization (SPC) parameters (i.e., annealing temperature and dwell time) on the resulting shape memory properties of NiTi sputtered thin films, while Gil *et al.*[16] examined the effect of grain size on martensitic phase transformation temperatures. Lee *et al.*[17,18] conducted a series of investigations into the kinetics of the SPC process via *in situ* transmission electron microscopy (TEM) observations. A wide variety of proposed SMA based actuation devices may be found in Refs. 19–22, again, all relying on homogeneous shape memory properties.

Several investigations on the use of laser annealing in order to control the spatial extents of crystalline regions have been conducted, although they have all been restricted to cw laser, solid-phase processing. Bellouard and co-workers[23,24] used a near IR cw laser to selectively solid-phase crystallize a sputter deposited NiTi thin film for the purposes of fabricating a microgripper whose only active component was the crystallized portion of the device. He *et al.*[25] investigated the use of a cw CO_2 laser to selectively anneal a NiTi thin film via SPC as well.

This work proposes the use of pulsed, melt-mediated laser crystallization techniques to control the spatial distribution of crystalline zones within an amorphous or precrystallized matrix. This process can provide not only spatial control over the shape memory response but through proper use of operational parameters has the potential for tailoring the

[a]Electronic mail: ajb2118@columbia.edu.

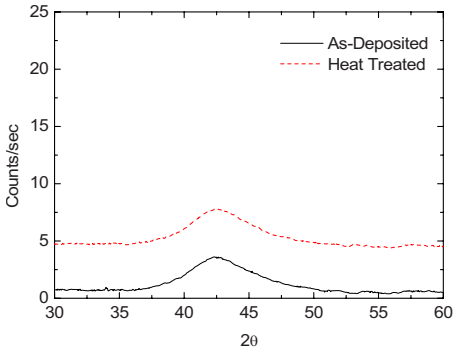

FIG. 1. (Color online) XRD spectrum of as-deposited film. Note the amorphous scattered signal indicative of room temperature sputtered NiTi. Heat treated spectrum shifted for clarity.

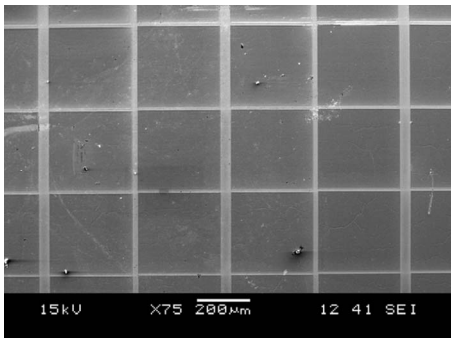

FIG. 2. SEM image of an array of irradiated regions. Irradiated regions are 320×320 μm^2 with uniform energy density. Each square region represents one energy density.

shape memory response itself, i.e., phase transformation temperature, transformation strain, recovery stress, etc. The use of a melt-mediated process also provides several advantages over homogeneous furnace annealing as well as cw, solid-phase techniques. These include increased efficiency for large scale fabrication due to single shot batch processing capabilities (i.e., no rastering), increased control over the resulting microstructure, and features with sharp boundaries between irradiated and adjacent unirradiated film areas. Crystallization rates for the pulsed process (approximately nanosecond pulse durations) also far exceed those of cw processing whose scan speeds are on the order of 3–5 mm/s and furnace annealing times ranging from tens of seconds to several hours. The pulsed process is also advantageous as it may be performed on device films *in situ* in fairly close proximity to other possibly thermally sensitive components.

II. EXPERIMENTAL SETUP

NiTi films were deposited by simultaneous cosputtering from an alloyed NiTi target and pure titanium target at powers of 302 and 50 W, respectively, for 300 s at an argon pressure of 3 mTorr resulting in films 200 nm in thickness. The films were deposited on a 1 μm ultralow residual stress silicon nitride (Si_3N_4) barrier layer that had been deposited on a [100] silicon wafer via low pressure chemical vapor deposition. The deposition was performed at room temperature and thus resulted in an amorphous film as confirmed by x-ray diffraction (XRD), as seen in Fig. 1. Furthermore, the film composition as Ni 52.4 at. % was obtained via a calibrated electron microprobe.

Prior to laser processing, for the films laser treated at room temperature, it was also necessary to subject the film to a preheat treatment in order to thermally oxidize the film surface to enhance optical absorption at the laser wavelength. Films were held at 400 °C for 1 min of oxide growth prior to laser irradiation. Lee *et al.*[17] suggested that SPC of the film will not occur for the above heat treatment parameters. However, as a precaution, XRD (see Fig. 1) conducted postheat treatment, confirming the film remained amorphous. Films were then single shot, pulse irradiated by a 308 nm wavelength, XeCl excimer laser with a 30 ns pulse duration over energy densities ranging from approximately 100–1110 mJ/cm^2. Energy density was uniform within the irradiated region whose geometry was a 320×320 μm^2. The laser system is synchronized with the underlying *XYZ* motion system such that a series of energy densities may be applied producing a spatial array on a single specimen. An array of irradiated regions may be seen in Fig. 2. Each square region is an irradiated area of a single uniform energy density with 10 μm spacing. In addition, the effects of laser processing at elevated substrate temperatures have also been investigated through the use of a hot stage with controlled atmosphere. Substrate temperatures as high as 800 °C are utilized while maintaining an inert atmosphere through argon flow in order to mitigate the effects of film oxidation. The heat treatment for each analyzed substrate temperature is as follows: films are heated at 100 °C/min to the desired temperature, and the specimens are held at that temperature for 1 min to ensure temperature stabilization prior to laser irradiation. Laser irradiation is then performed over the following minute, and the specimen cooled at maximum cooling rate, 30 °C/min.

III. THEORETICAL BACKGROUND

A. Nucleation and solidification

The underlying phenomena governing pulsed laser crystallization have their basis in highly transient heat flow and nonequilibrium solidification. The laser energy is coupled to the film via nonlinear absorption over, in this case a metallic matrix, a shallow near surface layer resulting in melting and resolidification. The extent of the melted region is determined by the incident laser energy, the optical and thermophysical properties of the material. Solidification is accompanied by a release of energy in the form of the latent heat of fusion, H_f, at the solid liquid interface, which further contributes to the thermal profile within the film. The transient temperature distribution is therefore governed by the classical heat equation:

$$\rho^i(\Phi,T^i)c_p^i(\Phi,T^i)\frac{\partial T^i}{\partial t} = \nabla[k^i(\Phi,T)\,\nabla\,T^i] + \Sigma Q_{\text{nuc}}(x,y,z,t) + Q_{\text{laser}}(x,y,z,n_i,k_i,\lambda), \quad (1)$$

where T^i, ρ^i, c_p^i, and k^i are the temperature, temperature dependent density, specific heat, and thermal conductivity, respectively, for the ith material and phase, Φ. $Q_{\text{nuc}}(x,y,z,t)$

are the energy contributions from latent heat of solidification and $Q_{\text{laser}}(x,y,z,\lambda)$ is the laser energy input that is actually coupled to the film, taking the optical properties of the material into account. Convection to the surroundings is not taken to account due to the time scale over which solidification occurs. This situation also makes it possible to assume that radiation is negligible compared with heat conduction through the film.

Depending on the details of solidification, the film may proceed via several distinct, highly nonequilibrium pathways.[2] Crystallization may proceed via regrowth, nucleation, and growth of solids. Nucleation, homogeneous or heterogeneous, occurs via the formation of "solid" embryos at temperatures below the equilibrium melting temperature of the material driven by the ultimate reduction in the system's Gibbs free energy. CNT models this phenomenon by assuming, in the case of homogeneous nucleation, the formation of a spherical embryo of radius, r, and for heterogeneous, a spherical cap of radius r in contact with a flat catalytic surface at a contact angle, θ, the difference in Gibbs free energy reaches some critical threshold. The change in Gibbs free energy (homogeneous) goes according to[26]

$$\Delta G^{\text{tot}} = \frac{4\pi}{3} r^3 \Delta G_v + 4\pi r^2 \sigma_s, \tag{2}$$

where ΔG_v is the difference in volumetric free energy between the liquid and solid (a negative quantity below the equilibrium melting temperature) and σ_s is the surface free energy per unit area (positive value) associated with the formation of a new solid/liquid interface for a spherical embryo. A critical size nucleus, r^*, is formed when the radius is large enough such that a further increase in size results in a decrease in the total Gibbs free energy. For homogeneous nucleation,

$$r^* = \frac{2\sigma_s}{\Delta G_v} \Rightarrow \Delta G^* = \frac{16\pi\sigma_s^3}{3\Delta G_v^2}. \tag{3}$$

The nucleation rate per unit volume at a given undercooling is

$$I = I_0 \exp\left(\frac{-\Delta G^*}{kT}\right), \tag{4}$$

where k is the Boltzmann constant, I_0 is a fairly complex kinetic prefactor related to the frequency with which "liquid" atoms attach to the embryo, and the exponential is the number of critical size embryos per unit volume. For heterogeneous nucleation, the details of the derivation are omitted but proceed similarly and are given as

$$r^* = \frac{2\sigma_s}{\Delta G_v}, \quad \Delta G^*_{\text{het}} = \Delta G^* S(\theta_c) = \frac{16\pi\sigma_s^3}{3\Delta G_v^2} S(\theta_c), \tag{5}$$

where $S(\theta_c)$ is a geometric factor taking the contact angle, θ_c, of the nucleus with the catalytic surface. It should be noted that $S(\theta_c) \leq 1$ and thus $\Delta G^*_{\text{het}} \leq \Delta G^*_{\text{hom}}$. Physically, this translates to a lower energy threshold to overcome for nucleation in the heterogeneous case, and, in fact, most metallic melts are dominated by heterogeneous nucleation.[5]

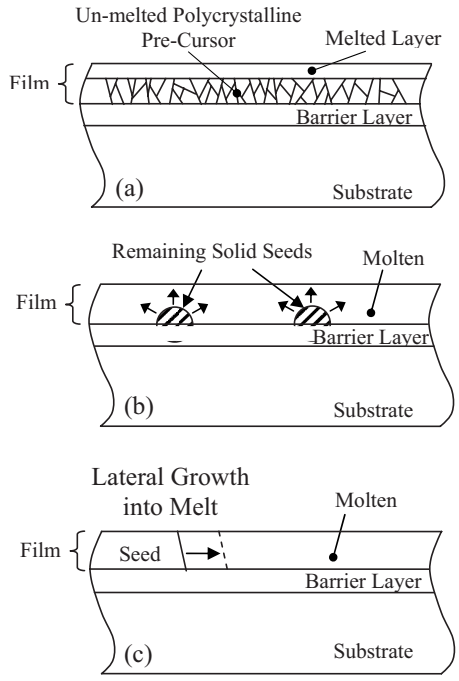

FIG. 3. Schematic representations of the (a) PM, (b) NCM, and (c) CM regimes.

Upon successful nucleation, nuclei will immediately begin to grow. While homogeneous nucleation or rapidly quenched films require significant undercooling, growth can occur at fractions of a degree below the equilibrium melting temperature.[23] Growth velocity is a strong function of temperature and is captured by the interface response function which relates the solid/liquid interface velocity to the interface temperature. For pure metallic melts, Turnbull suggested a collision limited theory resulting in

$$v_i = f v_s \left[1 - \exp\left(\frac{\Delta \bar{G}}{RT_i}\right)\right], \tag{6}$$

where v_s is the speed of sound in the melt and f represents the fraction of available site on the solid interface upon which liquid atoms may attach. Aziz[27] modified Eq. (6) for binary alloys by assuming that the driving force $\Delta \bar{G}$ is calculated via a weighted average of the chemical potentials of the constituents with respect to their compositions.

B. Thin film melting regimes

The process of thin film melting may be generally described by three distinct energy density regimes as developed by Im *et al.*[28] These regimes are defined by the extent to which the film has been melted through the thickness and are depicted schematically in Fig. 3. At low energy densities (relative to thermal, thermodynamic, as well as specimen configuration), the laser energy absorbed by the film is not sufficient to completely melt the film through the thickness. This range of energy densities is termed the *partial melting* (PM) regime. In this case, for precrystallized films, resolidification proceeds via vertical regrowth from the remaining unmelted solid seeds. For polycrystalline films whose initial grain size is less than the film thickness, microstructures in

this regime are characterized by grain sizes that remain on the order of the film thickness, and the substrate does not directly participate. For larger initial grain sizes relative to film thickness, their size after irradiation is not altered significantly due to the limited distances over which growth can occur.

At high energy densities, the energy provided by the laser is sufficient for complete through-thickness melting. This is the *complete melting* (CM) regime. For flood irradiated areas, solidification proceeds along two paths. The first is lateral epitaxial growth at the boundary of the irradiated area where adjacent solid seeds grow into the significantly undercooled melt resulting in long, high aspect ratio crystals. The other path is via nucleation and subsequent growth. This occurs away from the boundary of irradiation and results in planar, equiaxed grains. Microstructures in this regime thus consist of laterally grown grains at the boundary, and nucleated grains whose diameters can greatly exceed the film thickness.

The final regime is the *near complete melting* (NCM) regime, and as the name suggests occurs over energy densities through which PM transitions to complete melting. Due to local inhomogeneities, for energy densities near the complete melt threshold (CMT), there are portions of the film that are completely melted and portions that are only partially melted. In this case, solidification proceeds via two routes. The molten portions of the film go through nucleation and growth, while the near-complete melted seeds grow immediately upon reaching only slight undercoolings. The resulting grain size distribution is characterized by a bimodal character with small grains having resulted from nucleation and growth, and large grains stemming from the remaining solid seeds that had additional time for growth before being arrested by surrounding nucleants. As will be discussed in Secs. IV and V, the microstructures observed for an array of incident laser energies in this investigation are consistent with the above described melting regimes.

IV. RESULTS AND DISCUSSION

A. Optical absorption enhancement

Initial attempts at crystallizing an array of films with varying thickness and slight variations in composition over a wide range of energy densities were unsuccessful, i.e., no microstructure was detectable by either atomic force microscopy (AFM) or XRD. Figure 4 is taken from the investigation of Khelfaoui *et al.*[29] into the effects of laser induced oxidation of NiTi thin films. It is a plot of optical reflectivity as a function of wavelength for amorphous and oxidized NiTi films. It is clearly seen that optical reflectivity of the amorphous film drops precipitously due to the formation of a thin surface oxide. This decrease is particularly significant at 308 nm, which corresponds to the wavelength at which the specimen is processed. Thus, it was deduced that, initially, most of the incident laser energy was being reflected and most likely only melting a very thin, near surface layer. The growth of a thin oxide resulted in enhanced optical absorption, thus enabling the melting of the film. Figure 5 is a plot of intensity versus binding energy spectrum for the heat treated film obtained via x-ray photoelectron spectroscopy (XPS). It clearly shows the formation of intensity peaks at binding energies consistent with the formation of a layer of TiO_2.

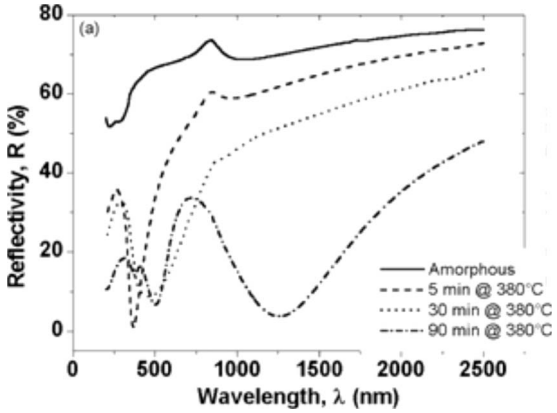

FIG. 4. Reflectivity spectrum for an amorphous and a number of heat treated films. This change in reflectivity, due to oxidation, particularly at $\lambda = 308$ nm, is consistent with observed enhanced laser-film energy coupling (Ref. 29).

B. Resultant phases

Laser irradiation of the films was initially performed over a range of energy densities with the substrate at room temperature. Employing the above mentioned method for optical absorption enhancement, the irradiated, initially amorphous regions of the film were crystallized.

Figure 6 contains a XRD spectrum of a room temperature irradiated specimen, confirming the presence of crystalline material. As will be discussed later, it was also determined that the film had undergone complete melting, and thus nucleation and growth in order to solidify. The amorphous spectrum is included for reference. The presence of a single peak implies a strong normal texture suggesting the film had undergone heterogeneous nucleation at the film-barrier layer interface.

Although crystallization was confirmed, after close scrutiny it was determined that the peak location for the crystallized film could not be indexed to either the martensite or austenite phase, and thus would not result in the desired shape memory response. Attempts to perform elevated temperature XRD also did not result in the emergence of any detectable austenitic peaks. The peak may be indexed to the

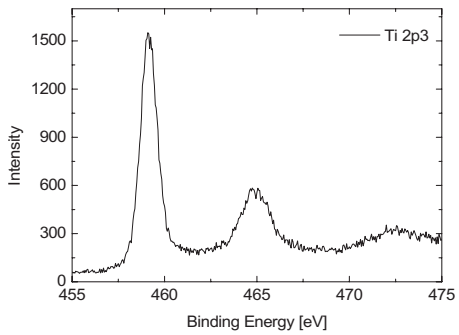

FIG. 5. XPS spectrum (Ti $2p3$) of heat treated film confirming presence of TiO_2.

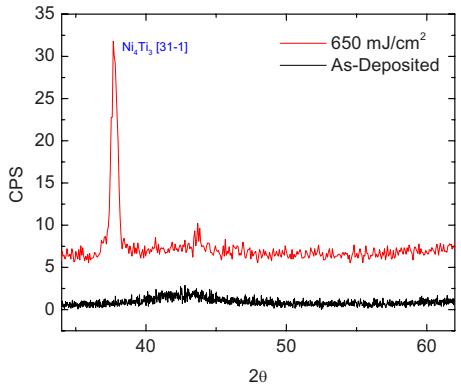

FIG. 6. (Color online) XRD spectra for the as-deposited amorphous spectrum and the room temperature, laser treated specimen (completely melted) confirming crystallization as well as heterogeneous nucleation. Additionally, it is seen that a metastable Ni_4 Ti_3 phase results due to the exceedingly high quench rate.

metastable Ni_4Ti_3 (Refs. 3–11) orientation. This is very likely due to the exceedingly high quench rate resulting from the pulsed laser process, which particularly for concentrated alloys can be expected to result in the formation of metastable phases.

Upon discovering that laser processing at room temperature did not result in viable shape memory material, it was determined that processing at elevated substrate temperatures, that is, preheating the specimen prior to and during laser irradiation, would significantly reduce the quench rate, and thus have added potential for resulting in the desired phase(s). It should be noted, however, that the preheating of the substrate actually results in SPC of the film *prior* to irradiation, and thus the crystallization process may no longer be seen as amorphous to crystal, but now SPC matrix to laser induced crystal. While this will impact the specimen treated at energy densities below the CMT, it may be seen as having no effect on nucleated crystals having resulted from laser processing within the CM regime as for both cases, the transformation proceeds from liquid.

Substrate temperatures ranging from room temperature to 800 °C were analyzed. It was seen that substrate temperatures below 600 °C resulted in the previously seen Ni_4Ti_3 obtained from room temperature processing. However, at 600 °C and above, significant changes in both the microstructure as well as the phase resulted.

Figure 7 contains XRD spectra collected from specimen laser treated at 600 °C. Upon heating the specimen to 140 °C, both the [110] and [200] austenitic peaks are present. After allowing the film to cool back down to room temperature, the [110] peak remains, but the [200] peak intensity decreases significantly. The specimen was then cooled with dry ice to −78 °C and allowed to heat back up to room temperature. This resulted in a complete disappearance of the [200] peak, although the [110] peak persisted. This persistence in the [110] orientation while the [200] peak recedes may be attributed to variations in the micromechanical stresses with individual grains due to anisotropic Young's modulus. This difference in stress effectively can effectively shift the phase transformation temperatures. Although no discernable martensitic peaks are detected, the appearance and

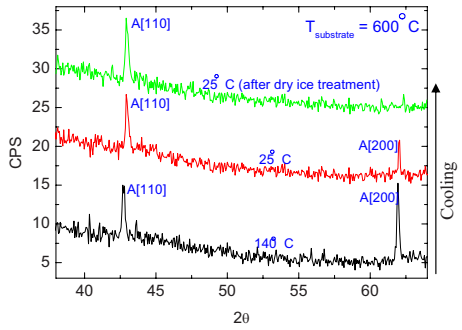

FIG. 7. (Color online) XRD spectra depicting the thermally induced phase transformation. Note that emergence of the austenitic phase upon heating and subsequent disappearance upon cooling. The persistence of the [110] austenitic peak suggests a phase mixture of austenite and martensite upon cooling back down to room temperature.

subsequent disappearance of the [200] austenite upon cooling are direct evidence of the martensitic transformation. The incomplete disappearance of the [200] peak upon cooling suggests that room temperature lies within the hysteresis defined by the alloy's transformation start and finish temperatures.

Figure 8 reveals the XRD spectra collected from specimen laser treated at room temperature and 800 °C, both processed at energy densities above their respective CMTs. The change in peak location is evident after having processed at an elevated temperature. This peak is indexed as [200] austenite. In addition, it should be noted that only a single peak appears, again implying that the film solidified via heterogeneous nucleation and growth. It should also be noted that the resulting normal crystallographic orientation is based on the overall energetic configuration of the molten liquid, amorphous substrate, and solid nucleus,[37] explaining the presence of the [200] austenite.

Upon observing that *in situ* XRD spectra from the 600 °C substrate case reveal a disappearance of the austenitic [200] orientation, but the 800 °C spectra remain unchanged, it is assumed that the effective phase transformation temperatures of the 600 °C case exceed those of the

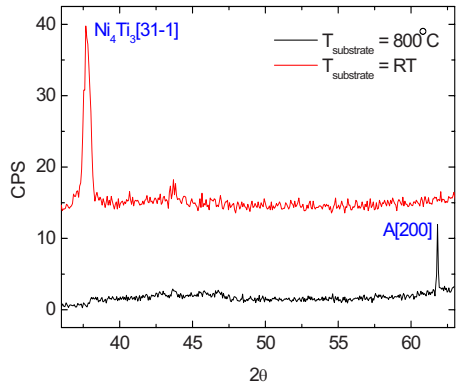

FIG. 8. (Color online) XRD spectra for room temperature and 800 °C substrate temperature. Room temperature processing (ED=650 mJ/cm^2) results in metastable phase formation, while an elevated substrate temperature processing (ED=682 mJ/cm^2) results in the formation of austenite. Note that both films were laser treated above their respective complete melt thresholds and result in highly textured films implying heterogeneous nucleation.

800 °C processed film. The apparent shift in martensitic phase transformation temperatures that results from processing at 600 °C versus 800 °C may be explained by a series of factors. Gil *et al.*[16] reported an inversely proportional phase transformation temperature dependence on grain size. As the quench rate for the 800 °C is lower than that of the 600 °C processed specimen, this decreases the nucleation rate and thus allows added time and available volume for growth into the melt. Grain sizes from the 800 °C film are, in fact, larger than their 600 °C counterpart. Another factor that must be considered is the incorporation of oxygen into the film due to the preheating process. Although the hot stage specimen chamber was purged and continuously subjected to argon flow, oxidation was observed as a change in surface color from silver to gold. The color change was more severe at higher preheat temperatures due to the increased oxidation rate. Otsuka and Wayman[30] reported significant decreases in phase transformation temperatures as a function of oxygen content. This increased oxygen level in the film is consistent with observing austenite at room temperature for the films treated at 800 °C.

V. MECHANICAL AND SHAPE MEMORY/ SUPERELASTIC RESPONSE

A. Recoverable energy

In addition to examining the melt and solidification process, a characterization of the load response via nanoindentation of laser treated specimen has also been performed over a range of energy densities and substrate temperatures. All presented indentations were performed with an Agilent Nanoindent® G200 platform with a three-sided pyramidal Berkovich tip.

In performing and analyzing nanoindentation experiments performed on shape memory materials, it is crucial that one takes into account their highly nontraditional constitutive response. Significant complications arise due to the presence of multiple possible deformation mechanisms being active upon loading *and* unloading. Upon loading, in addition to the elastic response, additional inelastic responses include plastic deformation via dislocation motion in the parent and/or martensitic phase, the stress induced martensitic phase transformation, and/or martensitic twin reorientation.[31] Upon unloading, strain may also be recovered via elastic mechanisms in both the parent and martensite phases as well as the reverse stress induced martensite to austenite phase transformation. At sufficiently large indentation depths, further complexity appears due to contributions in the load response from the barrier layer/substrate. However, Fischer-Cripps[32] stated that it is a common practice to use ultimate indentation depths on the order of 10% of the film thickness in order to state with confidence that the response is film dominated.

In order to treat the added complexities introduced by the material, several authors[33,34] chose to use the recoverable energy upon unloading as a metric for comparison. The recoverable energy upon unloading includes both elastic contributions from the parent and the stress induced martensitic

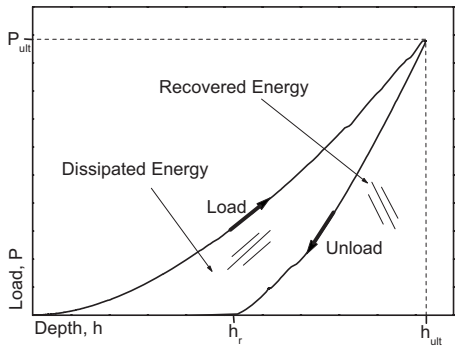

FIG. 9. Schematic load curve for typical nanoindentation experiment. Note that the total energy input to the system is equal to the sum of the dissipated and recovered energy.

phases and the superelastic response from the reverse transformation. Using Fig. 9 as reference, it is seen that the total energy input to the system upon loading is

$$W_{\text{tot}} = \int_0^{h_{\text{ult}}} P dh \tag{7}$$

and the energy recovered upon unloading, the area under the unloading portion of the film, is calculated as

$$W_{\text{rec}} = \int_{h_{\text{ult}}}^{h_{\text{res}}} P dh. \tag{8}$$

A recoverable energy ratio, η, may then be defined as the ratio of recovered to total input energy:

$$\eta = \frac{W_{\text{rec}}}{W_{\text{tot}}}. \tag{9}$$

Figure 10 shows the load response curves for specimens processed at room temperature, 600 °C, and 800 °C. They are presented such that they all have comparable ultimate indentation loads, though significant differences in behavior are seen. It is seen that all three differ significantly in ultimate depth, unloading slope, and residual depth. Within the context of the XRD spectra presented earlier, several observations can be made. It was shown earlier that the films processed at 600 °C and 800 °C are martensitic and austenitic at room temperature, respectively. This is manifested as

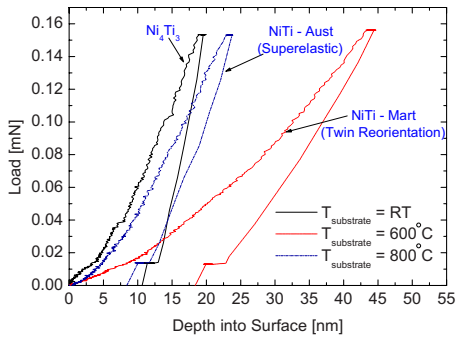

FIG. 10. (Color online) Load curve comparisons between specimens processed at room temperature (ED=650 mJ/cm^2), 600 °C (ED =643 mJ/cm^2), and 800 °C (ED=682 mJ/cm^2). Note that all specimens presented here were laser treated with energy densities above their respective CMTs.

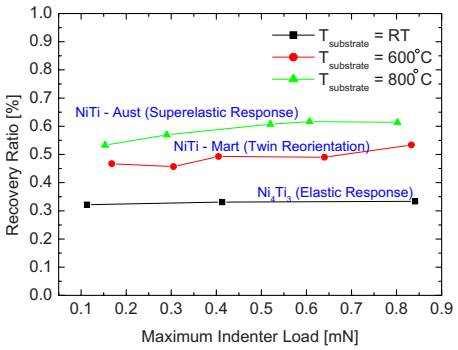

FIG. 11. (Color online) Energy recovery ratio as a function of maximum indenter load for films laser processed at room temperature (ED $=650$ mJ/cm^2), 600 °C (ED$=643$ mJ/cm^2), and 800 °C (ED $=682$ mJ/cm^2). It is seen here that the film processed at 800 °C recovers significantly more energy upon unloading due to its superelastic response. Note that all specimens presented here were laser treated with energy densities above their respective CMTs.

a significantly larger residual depth for the martensitic film due to inelastic martensitic twin reorientation, as opposed to the enhanced depth recovery due to the superelasticity for the austenitic film. The relative ease with which twin reorientation is also noted and manifested by the significantly increased ultimate depth required to generate a comparable indenter load.

Figure 11 is a plot of the recoverable energy ratio as a function of ultimate applied indenter load for specimen laser treated at room temperature, 600 °C and 800 °C. All three specimens have been treated with energy densities above their corresponding CMTs. It is seen that the specimens treated at 600 °C and 800 °C recover significantly more energy upon unloading than that processed at room temperature. It has already been confirmed via XRD that the specimen processed at 800 °C is austenitic at room temperature and thus exhibits a superelastic response, explaining the ability to recover the most energy upon unloading. This enhanced energy recovery is also consistent with the examination of Gall *et al.*[31] which showed that the [200] austenite surface normal orientation is particularly effective in recovering energy upon unloading. It was shown above via XRD that the film processed at 800 °C does indeed have a strong [200] normal texture due to having been heterogeneously nucleated. In addition, the solid-phase crystallized, untreated film only shows a 42% energy recovery. Thus manipulating the film's microstructure to result in a strong [200] normal texture has significantly increased the ability to recover energy and holds compelling implications for wear resistance applications.

XRD also revealed that the specimen processed at 600 °C is a phase mixture of austenite and martensite upon cooling from the fully austenitic state. This decrease in recoverable energy relative to that processed at 800 °C is explained by a corresponding increase in energy dissipated through martensitic twin reorientation while loading. A slight increase in the ratio is seen as the maximum load increases for the specimens processed at 600 °C and 800 °C. This could be due to an increase in elastic contribution from the underlying barrier layer. However, since the room temperature treated specimen does not show a corresponding increase at comparable load, it is also possibly due to the increased recovery from the reverse transformation relative to that dissipated by plastic flow.

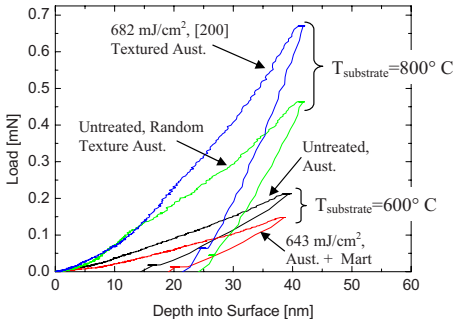

FIG. 12. (Color online) Load responses of laser treated and untreated films for elevated substrate temperatures of 600 °C and 800 °C. Note the increased slope as well as increased depth recovery for the laser treated, [200] textured film treated at 800 °C. The load response of a precrystallized (no laser treatment) film at 800 °C is also included for reference.

B. Effective film modulus

In addition to examining the recoverable energy ratio, the elastic response was also characterized via the more traditional elastic unloading analysis. However, it is stressed that the elastic moduli presented here represent an *effective* film modulus. This effective modulus, as explained above, is the manifestation of several deformation mechanisms operating simultaneously upon unloading.

From the Hertz derivation, it is seen that the *reduced* modulus which accounts for the properties of both the film and indenter is given by

$$\frac{1}{E_r} = \frac{(1-\nu_f^2)}{E_f} + \frac{(1-\nu_i^2)}{E_i}, \tag{10}$$

where ν_f and E_f and ν_i and E_i are the Poisson ratios and Young moduli of the film and indenter, respectively. E_r may be obtained from the experimentally obtained load curve by utilizing the expression derived by Oliver and Pharr[35] for conical indenters:

$$E_r = \frac{S}{2\beta}\sqrt{\frac{\pi}{A}}, \tag{11}$$

where $S=dP/dh$ is the initial slope of the unloading curve, β is a geometric factor, in this case equaling 1.034 (Berkovich indenter), and A is the projected area of contact at the ultimate measured depth. Using the known properties of the indenter, $E_i=1141$ GPa and $\nu_i=0.07$, and assuming a Poisson ratio of 0.35 for the film, it is then possible to calculate the effective film modulus from Eqs. (10) and (11).

Load curves at comparable ultimate indentation depths for the 600 °C and 800 °C substrate temperature conditions, unprocessed and laser treated, are presented in Fig. 12.

For the 600 °C case, it is seen that the untreated austenitic film results in lower residual depths due to the superelastic strain recovery, while the laser treated martensitic film requires less indenter load to achieve a comparable indentation depth due to the relative ease with which martensitic

Substrate Temp.	Process Condition	Effective Modulus
RT	Amorphous, As-Deposited	224 ± 34 [Gpa]
	Laser Treated*	260 ± 34 [Gpa]
600° C	Untreated	61 ± 6 [Gpa]
	Laser Treated*	44 ±1 [Gpa]
700° C	Untreated	106 ± 7 [Gpa]
	Laser Treated*	112 ± 6 [Gpa]
800° C	Untreated	136 ± 22 [Gpa]
	Laser Treated*	171 ± 19 [Gpa]

FIG. 13. Effective film modulus for films laser processed at room temperature (ED=650 mJ/cm^2), 600 °C (ED=643 mJ/cm^2), and 800 °C (ED =682 mJ/cm^2). Effective film moduli for precrystallized (no laser treatment) and amorphous films are also included for reference. The asterisk (*) denotes that laser treated specimen presented here have undergone CM, and thus nucleation and growth in order to solidify.

twin variants may be reoriented. The 800 °C case differs in that both the untreated and laser processed films are both austenitic. However, it was shown in the discussion above that due to having been heterogeneously nucleated, the laser processed film results in a strong [200] texture. This is manifested as an increase in the unloading slope of the curve, as well as enhanced depth and energy recovery due to the anisotropy of the response.

The effective elastic moduli calculated from the load responses are summarized in Fig. 13. For clarification, the "untreated" properties presented in the figure are effective moduli of films that have been preheated, and thus solid-phase crystallized, but have not been laser treated. All of the laser treated properties presented in Fig. 13 are from regions that have undergone complete melting, and therefore nucleation and growth. The untreated values of effective modulus for the 600 °C, 700 °C, and 800 °C preheated and solid-phase crystallized films are those of randomly textured austenite as confirmed by XRD (not shown). However, the untreated effective modulus values increase as a function of preheat temperature. This is most likely due to the increases in surface oxidation with increased preheat temperatures. Increased oxidation rates result in thicker surface oxides which result in an enhanced contribution to the load response, particularly at shallow indentation depths. Thus comparisons should be made between treatments at comparable preheat temperatures. The 700 °C and 800 °C both show qualitatively similar results in that the laser treated films result in increased effective modulus. This is explained by the anisotropic dependence on both elastic modulus and transformation stress. The initial solid-phase crystallized films have a relatively random texture, whereas the films that have been treated above their CMT result in strong normal textures due to their having solidified via heterogeneous nucleation. The film processed at 600 °C actually shows a substantial decrease in effective modulus. This is due to a shift in phase transformation temperature resulting in an alloy that is martensitic at room temperature in contrast to the films treated at 700 °C and 800 °C.

C. Microstructure

Substrate temperatures ranging from room temperature to 800 °C were analyzed. Figures 14(a) and 14(b) are representative micrographs obtained via AFM from films laser processed at room temperature revealing the resulting microstructure as may be seen at the film surface. Figure 14(b) reveals laterally grown crystals indicating that the film has gone through complete melting. Figure 14(a) was obtained from the interior of the irradiated region and thus represents the microstructure of nucleated grains. It should be noted that films processed at temperatures below 600 °C result in similar microstructures, as well as microstructural trends as a function of incident energy density.

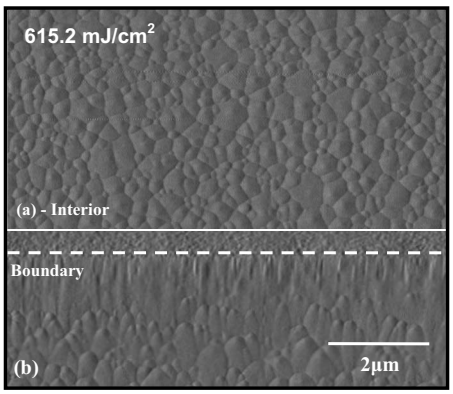

FIG. 14. [(a) and (b)] $T_{substrate}$=room temperature: representative AFM image from completely melted film. Note the presence of lateral growth, although not well defined or of significant length, ED=615.2 mJ/cm^2.

However, at 600 °C and above, significant changes in both the microstructure and the phase resulted. Figures 15(a)–15(f) are micrographs obtained via SEM for specimens processed at 800 °C. Figures 15(a), 15(c), 15(e), 15(b), 15(d), and 15(f) are obtained from laser treated areas away from and at the boundary of irradiation, respectively. The microstructures presented in these figures have also been quantitatively analyzed, and both grain size and representative grain size distributions as a function of %CMT are found in Fig. 16. The CMT was determined via the onset of well defined lateral growth at 596 mJ/cm^2. The three sets of micrographs are also representative of the microstructures resulting from processing at energy densities within the three thin film melting regimes discussed earlier. Although the micrographs presented here are limited to the 800 °C substrate case, the 600 °C and 700 °C microstructures have been analyzed, and follow the same phenomenological trend (i.e., PM, NCM, and CM transitions). However, it should be noted that, as can be expected from thermal and thermodynamic considerations, there are differences in actual grain sizes and shifts in CMT due to the variation in substrate temperature.

Figures 15(a) and 15(b) are micrographs representative of the resulting microstructures processed at energy densities within the PM regime. This is seen by the reduced grain size, i.e., grain sizes restricted by film thickness, as well as the fact that no lateral growth is present at the irradiated boundary. The detail provided in Fig. 16 at 78% CMT reveals an average grain size and distribution. Figures 15(c) and 15(d) are micrographs obtained from specimen laser treated at 99% of the CMT. A significant increase in average grain size, as well as a transition to a bimodal grain size distribution, is in both the micrographs and detail in Fig. 16. In addition, the presence of some lateral growth is seen at the boundary as may be expected in the NCM regime. Finally, Figs. 15(e) and

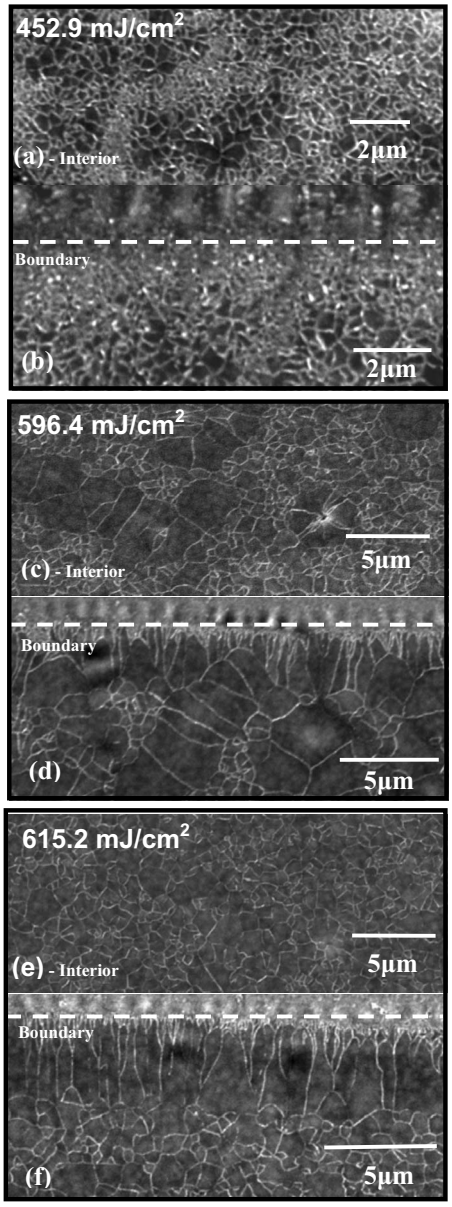

FIG. 15. Scanning electron micrographs, $T_{substrate}$=800 °C: [(a) and (b)] interior and boundary regions, respectively. Partially melted film characterized by small grain size limited to film thickness, ED=452.91 mJ/cm^2: [(c) and (d)] interior and boundary regions, respectively. NCM regime characterized by bimodal grain size distribution, ED=596.4 mJ/cm^2: [(e) and (f)] interior and boundary regions, respectively. Completely melted film characterized by the presence of large aspect ratio, well defined lateral growth, ED=615.2 mJ/cm^2.

15(f) are micrographs from specimen laser treated at 102% of CMT. Average grain size diminishes substantially, and the character of the grain size distribution changes to a single mode, log-normal distribution (see detail in Fig. 16). Most importantly, however, is the presence of well defined lateral growth at the boundary which is a direct evidence of film having undergone complete melting, and therefore nucleation and growth.[2,36]

VI. CONCLUSION

It has been shown that laser processing of films at elevated temperatures through the use of preheated substrates has a dramatic influence on their microstructure, phase, mechanical, and shape memory responses. Furthermore, it has been demonstrated that laser crystallization of precrystallized randomly textured austenitic films results in strong normal textures that are favorable with respect to energy recovery having strong implications for wear resistance applications. In terms of application, the requirement for preheated substrates does present some drawbacks, such as oxidation and potential incompatibility with temperature sensitive substrates. It also prevents the user from crystallizing within an amorphous matrix, as the preheat results in solid-phase crystallization. However, it has also been shown that laser processing at room temperature results in the production of non-shape memory phases. Thus a shape memory subtractive process may be implemented on crystalline films in order to spatially control the presence of shape memory responses. Additionally, techniques such as combining laser irradiation while utilizing a focused flash lamp to heat the film over microsecond time scales can enable the reduced quench rate required for desired phase formation, while maintaining the film's amorphous as-deposited state. Furthermore, future efforts will also include a deeper analysis of the resulting microstructure via TEM, as subgrain structures of laser processed films were observed via SEM but were not directly addressed in this work.

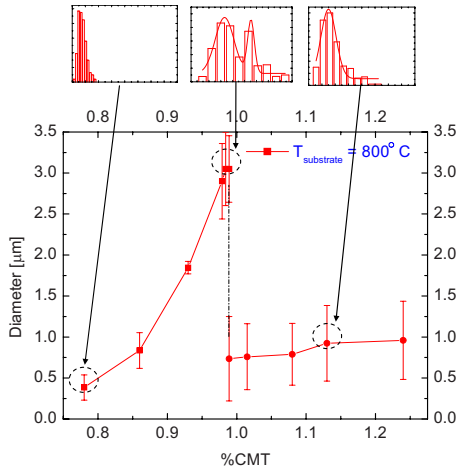

FIG. 16. (Color online) Average grain size as a function of % CMT. Note the evolution of grain size distribution as the energy density transitions through the PM, NCM, and CM regimes.

[1]T. Sameshima and S. Usui, Mater. Res. Soc. Symp. Proc. **71**, 435 (1986).
[2]J. S. Im, H. J. Kim, and M. O. Thompson, Appl. Phys. Lett. **63**, 1969 (1993).
[3]C. J. Lin and F. Spaepen, Acta Metall. **34**, 1367 (1986).
[4]J. S. Im, M. A. Crowder, R. S. Sposili, J. P., Leonard, H. J. Kim, J. H. Yoon, V. V. Gupta, H. Jin Song, and H. S. Cho, Phys. Status Solidi A **166**, 603 (1998).
[5]J. P. Leonard, Ph.D. thesis, Columbia University, 2000.
[6]C.-J. Lin, F. Spaepen, and D. Turnbull, J. Non-Cryst. Solids **61–62**, 767 (1983).
[7]C.-J. Lin and F. Spaepen, Mater. Res. Soc. Symp. Proc. **28**, 75 (1984).
[8]F. Spaepen, High Temp. Mater. Processes (N.Y., NY, U.S.) **7**, 91 (1986).
[9]C. S. Hau-Riege, S. P. Hau-Riege, and C. V. Thompson, J. Electron. Mater. **30**, 11 (2001).
[10]D. Y. Li, Wear **221**, 116 (1998).
[11]S. Gialanella, G. Ischia, and G. Straffelini, J. Mater. Sci. **43**, 1701 (2008).
[12]L. Tan, W. C. Crone, and K. Sridharan, J. Mater. Sci. Mater. Med. **13**, 501 (2002).

[13]A. Ishida and M. Sato, Acta Mater. **51**, 5571 (2003).
[14]A. Ishida, A. Takei, M. Sato, and S. Miyazaki, Mater. Res. Soc. Symp. Proc. **360**, 381 (1995).
[15]A. Ishida, A. Takei, M. Sato, and S. Miyazaki, Thin Solid Films **281–282**, 337 (1996).
[16]F. J. Gil, J. M. Manero, and J. A. Planell, J. Mater. Sci. **30**, 2526 (1995).
[17]H.-J. Lee, H. Ni, D. T. Wu, and A. G. Ramirez, Appl. Phys. Lett. **87**, 124102 (2005).
[18]H.-J. Lee and A. G. Ramirez, Appl. Phys. Lett. **85**, 1146 (2004).
[19]E. Makino, T. Mitsuya, and T. Shibata, Sens. Actuators, A **79**, 128 (2000).
[20]E. Wibowo, C. Y. Kwok, and N. H. Lovell, Proc. SPIE **5276**, 351 (2004).
[21]B. Selden, K. Cho, and H. Asada, Smart Mater. Struct. **15**, 642 (2006).
[22]E. Makino, T. Mitsuya, and T. Shibata, Sens. Actuators, A **79**, 251 (2000).
[23]X. Wang, Y. Bellouard, and J. J. Vlassak, Acta Mater. **53**, 4955 (2005).
[24]Y. Bellouard, T. Lehnert, J.-E. Bidaux, T. Sidler, R. Clavel, and R. Gotthardt, Mater. Sci. Eng., A **273-275**, 795 (1999).
[25]Q. He, M. H. Hong, W. M. Huang, T. C. Chong, Y. Q. Fu, and H. J. Du, J. Micromech. Microeng. **14**, 950 (2004).
[26]D. A. Porter and K. E. Easterling, *Phase Transformations in Metals and Alloys* (Van Nostrand Rheinhold, Berkshire, England, 1981).
[27]M. J. Aziz, J. Appl. Phys. **53**, 1158 (1982).
[28]J. S. Im, H. J. Kim, and M. O. Thompson, Appl. Phys. Lett. **63**, 1969 (1993).
[29]F. Khelfaoui, Y. Bellouard, T. Gessmann, X. Wang, J. Vlassak, and M. Hafez, SMST 2004, Baden-Baden, Germany (unpublished).
[30]K. Otsuka and C. M. Wayman, *Shape Memory Materials* (Cambridge University Press, Cambridge, UK, 1998).
[31]K. Gall, K. Juntunen, H. J. Maier, H. Sehitoglu, and Y. I. Chumlyakov, Acta Mater. **49**, 3205 (2001).
[32]A. C. Fischer-Cripps, *Nanoindentation*, 2nd ed. (Springer-Verlag, New York, 2004).
[33]R. Liu and D. Y. Li, Scr. Mater. **41**, 691 (1999).
[34]W. Ni, Y. Cheng, and D. S. Grummon, Surf. Coat. Technol. **177–178**, 512 (2004).
[35]W. C. Oliver and G. M. Pharr, J. Mater. Res. **7**, 1564 (1992).
[36]J. S. Im and H. J. Kim, Appl. Phys. Lett. **64**, 2303 (1994).
[37]J. W. Cahn and J. E. Taylor, in *Phase Transformations*, edited by G. Lorimer (Institute of Metals, London, 1989), pp. 545–561.